Journal of Materials Chemistry A

ROYAL SOCIETY OF CHEMISTRY

PAPER

View Article Online
View Journal

Cite this: DOI: 10.1039/d5ta09289b

Cerium-doping and nitridation effects on nickel-based metal organic frameworks for alkaline water oxidation

Chikaodili E. Chukwuneke, [ad] Kenta Kawashima, [a] Tran Phuoc Anh Nguyen, [a] Gabriella Ruiz, [a] Johnpaul Smith, [a] Raul A. Marquez, [a] Jay T. Bender, [b] Jing Lian Ng, [b] Xun Zhan, [b] Wennie Wang, [bcd] Delia J. Milliron, [abcde] Michael J. Rose [ad] and C. Buddie Mullins *[abcde]

In the quest for a green energy future, renewable energy-driven hydrogen production *via* alkaline water electrolyzers leads toward a sustainable human society. However, the complementary oxygen evolution reaction (OER) in alkaline water electrolysis limits the overall electrolyzer efficiency since it requires complex, multi-step electron transfer. This work introduces a synthetic strategy that translates a less-conductive Ce-doped nickel metal–organic framework (MOF) into a conductive precatalyst (*i.e.*, a Ce-doped nickel nitride and carbon-based composite) through nitrogen incorporation. Nitrogen incorporation leads to the formation of a nitride phase, and a carbon-based material phase, while the Ce^{3+} species leads to the formation of pseudo-tetrahedral geometries at Ni sites, which enhances OER kinetics, as indicated by a Tafel slope of 83.6 mV dec^{-1}. Nitridation led to an approximately 50× improvement in OER activity relative to the parent MOFs. Moreover, cerium doping and nitridation produced a synergistic effect, with $Ce_{0.03}Ni_{0.97}$-NMOF achieving a faradaic efficiency of 100% and maintaining stable operation for 24 hours at a current density of 10 mA cm^{-2}, exhibiting even higher activity after prolonged testing.

Received 14th November 2025
Accepted 16th March 2026

DOI: 10.1039/d5ta09289b

rsc.li/materials-a

Introduction

Energy is essential for productive living on any planet in the "Milky Way", and as human technologies continue to advance, more of it is needed. Intermittent energy sources such as solar, wind, and hydropower offer opportunities but face the downside of being occasionally intermittent. One of the ways of ensuring energy efficiency and curbing waste from sporadic fuel sources is by storing them in chemical bonds through energy conversion devices. In recent times, water-splitting technologies have been on the front burner to ensure a sustainable and green source of hydrogen production. For hydrogen production to be industrially efficient, catalyzing the oxygen evolution reaction (OER), a complementary reaction of hydrogen production from water in an electrochemical cell, is essential to lower its overall energy requirement.

Electrocatalysts are employed to lower the energy requirement per product, and classes of materials such as metal–organic frameworks (MOFs) have been utilized owing to their superior high surface area, flexible structure, high porosity, and high tunability owing to the numerous possible combinations of ligands and metal salts.[1,2] Despite the promising catalytic properties MOFs possess, they have a major drawback of poor electron transport due to the insulating nature of the organic linkers and instability under OER conditions.[3–5] This challenge has inspired innovative approaches to transforming non-conductive MOFs into conductive precatalysts, which undergo *in situ* transformation into metal oxide OER catalysts,[6,7] with improved electrical conductivity, while capitalizing on their advantages.[8]

In transforming the MOFs into better precatalysts, synthetic designs leading to derived metal nanoparticles,[9–14] oxides,[15–19] chalcogenides,[20–30] and phosphides[31–37] have been studied; however, nitrides have not been well studied. In fact, the literature shows only one investigation of a MOF-derived nitride precatalyst[38] and a drawback of the extant synthetic strategy is the conductivity and surface area penalty associated with the carbon framework lost during the process.[11] Another technique for making MOF-derived precatalysts more active is cation doping (*e.g.*, Ce), which has been demonstrated to help create active sites by modifying the material's electronic structure, leading to enhanced conductivity and stabilization of OER intermediates.[39–42]

[a]*Department of Chemistry, College of Natural Sciences, The University of Texas at Austin, Austin, Texas 78712, USA. E-mail: mullins@che.utexas.edu*

[b]*McKetta Department of Chemical Engineering, The University of Texas at Austin, Austin, Texas 78712, USA*

[c]*Texas Materials Institute, The University of Texas at Austin, Austin, Texas 78712, USA*

[d]*Allen J. Bard Center for Electrochemistry, The University of Texas at Austin, Austin, Texas 78712, USA*

[e]*H2@UT, The University of Texas at Austin, Austin, Texas 78712, USA*

Here, we outline a site engineering strategy by employing nitridation and doping techniques. In this study, we doped the parent Ni-MOF (called Ce_0Ni_1-MOF) with 1, 3, and 5% Ce ($Ce_{0.01}Ni_{0.99}$-MOF, $Ce_{0.03}Ni_{0.97}$-MOF, and $Ce_{0.05}Ni_{0.95}$-MOF, respectively) after which nitridation aided the formation of nickel nitride species. We demonstrate that nitridation can selectively incorporate nitrogen into the lattice structure of nickel in a MOF structure while retaining the carbon framework. The resulting nickel nitride phase and carbon framework aided conductivity, while Ce-doping is hypothesized to create a pseudo-tetrahedral geometry on nickel sites, which aids the OER. We also provide a molecular structure hypothesizing the existence of a pseudo-tetrahedral geometry on the nickel sites due to Ce-doping, which, to the best of our knowledge, hasn't been reported for MOF-derived precatalysts for the OER. Our results show that the combined site design techniques improved the electrochemical activity of the precatalyst relative to the parent MOF.

Experimental methods

Materials

Nickel nitrate hexahydrate (99% purity, Thermo Scientific), cerium nitrate hexahydrate (99% purity, Sigma Aldrich), terephthalic acid (TPA) (98% purity, Sigma Aldrich), NaOH (97% purity, Sigma Aldrich), KOH (90% purity, Sigma Aldrich), isopropanol (99.5% purity, Sigma Aldrich), dimethylformamide (DMF) (99.8%, Fisher chemicals), and ammonia gas (Airgas) were used for electrode synthesis and electrochemical reactions.

Electrocatalyst synthesis

Synthesis of Ni-MOF and Ce-doped Ni-MOF precursors. Ni-MOF (called Ce_0Ni_1-MOF) was synthesized by following a modified method[43] in which 96 mg of $Ni(NO_3)_2$, 166 mg of TPA, and 20 mL of DMF were mixed. This was followed by the dropwise addition of 2 mL of 400 mM NaOH while stirring the mixture for 30 minutes. NaOH facilitates the deprotonation of the carboxylic acid groups in the organic linker and adjusts the solution pH, thereby enabling the coordination of Ni^{2+}/Ce^{3+} ions with terephthalate anions and promoting MOF crystallization. The Ce-doped Ni-MOFs ($Ce_{0.01}Ni_{0.99}$-MOF, $Ce_{0.03}Ni_{0.97}$-MOF, and $Ce_{0.05}Ni_{0.95}$-MOF) were prepared on a Ni : Ce mole ratio basis by following the same method as described for the synthesis of the bulk Ni-MOF with the addition of 1, 3, and 5 moles % Ce $(NO_3)_3 \cdot 6H_2O$. After the addition of Ce salt, DMF was added followed by stirring, and addition of 2 mL of 400 mM NaOH in that order before it was transferred to the reactor for the solvothermal reaction in the furnace. The furnace was ramped to 100 °C at 5 °C min^{-1} and maintained at the final temperature for a total time of 8 h. After synthesis, the MOF was washed with DMF and ethanol sequentially before centrifugation and allowed to dry overnight at 60 °C in a vacuum oven. The synthesis resulted in a pure Ni-MOF yield of ~92.4%.

Synthesis of MOF-derived Ni_3N and Ce-doped Ni_3N precatalysts. The as-synthesized Ce_0Ni_1-MOF was converted into a composite of nickel nitride (Ni_3N) and carbon framework by flowing NH_3 gas over 100 mg of Ce_0Ni_1-MOF at a flow rate of 50 sccm at varying temperatures (300–450 °C) in a horizontal tube furnace, arriving at an optimized temperature of 350 °C. The Ce_0Ni_1-MOF was heated from room temperature to the optimized temperature at a ramp rate of 5 °C min^{-1} and held for another for 1 h, all under an ammonia atmosphere. During the cooling phase, when the temperature dropped below 100 °C, the gas flow was switched from NH_3 to N_2 to maintain an inert environment, resulting in the formation of a MOF-derived Ni_3N electrocatalyst. Similarly, the MOF-derived Ce-doped Ni_3N electrocatalysts ($Ce_{0.01}Ni_{0.99}$-NMOF, $Ce_{0.03}Ni_{0.97}$-NMOF, and $Ce_{0.05}Ni_{0.95}$-NMOF) were prepared by following the same method as described in the synthesis of the MOF-derived Ni_3N precatalyst but at the optimized temperature obtained from its synthesis. The synthesis resulted in a composite yield of 72.4%.

Characterization

The crystallinity of the resultant Ce_0Ni_1-MOF and Ce-doped Ni MOFs, and their corresponding nitrides were characterized with a Rigaku MiniFlex 600 X-ray diffractometer with a Cu Kα radiation (λ = 1.54186 Å) source to obtain the X-ray diffraction patterns (XRD) of the materials. An Apreo 2 C LoVac scanning electron microscope (SEM) with a Bruker energy dispersive X-ray detector (EDX) was used to investigate the precatalysts' morphologies and bulk elemental composition. Surface compositions of the samples were evaluated using a PHI Versaprobe4 X-ray photoelectron spectrometer (XPS) with Mg Kα1 radiation ($h\nu$ = 1253.7 eV). Fourier-transform infrared spectroscopy (FTIR) was used to evaluate the functional groups and was performed using an InvenioR system. Transmission electron microscope (TEM) images were obtained using a JEOL NeoARM system. 7500ce quadrupole inductively coupled plasma mass spectrometry (ICP-MS) was used to evaluate the metal content of the precatalyst.

Electrochemical measurements

Electrochemical reactions were performed using a CHI 608D potentiostat coupled to a three-electrode setup in a Teflon cell. The three-electrode setup consists of a graphite counter electrode, a Hg/HgO reference electrode (internal solution: 1 M KOH), the as-prepared loaded glassy carbon electrode as the working electrode, and 1 M KOH aqueous solution as the electrolyte. Here, the working electrode was prepared *via* a drop-casting method (catalyst loading amount: 0.3 mg cm^{-2}). The ink was prepared by dissolving 2.5 mg of the sample in 1 mL of ~0.05 wt% Fumion (dissolved in isopropanol). To remove O_2 bubbles during the electrochemical tests, a rotating disk electrode (RDE, Pine Instrument) system was used (rotating speed: 1600 rpm). All measurements were converted from V *vs.* Hg/HgO to V *vs.* the reversible hydrogen electrode (RHE) using the Nernst equation:[44]

$$E_{RHE} = E_{Hg/HgO} + 0.0592 \times pH + E^{\circ}_{Hg/HgO}$$

$$E^{\circ}_{Hg/HgO}(1M\ KOH) = 0.1053\ V \text{ at } 25^{\circ}C$$

The electrochemical behavior of the resultant nitride pre-catalysts was evaluated using the following electrochemical protocol. First, the precatalysts were activated using CV cycles at a scan rate of 5 mV s^{-1} until three consecutive replicate CVs were obtained. The three consecutive replicate CVs indicate that the catalytic surface is stable. Immediately after activation, electrochemical impedance spectroscopy (EIS) was utilized to obtain the uncompensated resistance (R_u) and the charge transfer resistance (R_{ct}) using an applied voltage of 0.70 V *vs.* Hg/HgO. In addition, EIS was utilized to obtain the double layer capacitance value (C_{dl}) by using the equation

$$C_{dl} = CPE_{ct} \times (\omega_{max})^{n-1}$$

where CPE_{ct} represents the charge transfer resistance of the constant phase element, ω_{max} stands for the maximum frequency of the imaginary component of the Nyquist plot, and n defines the deviation from ideal capacitance.

Next, the surface of the electrocatalysts was completely oxidized using chronopotentiometry (CP) at a current density of 2.5 mA cm^{-2} for 10 minutes (see Fig. S21) to ensure that the current response while measuring the Tafel slope can be ascribed to OER currents only. Subsequently, MUSCP was used to obtain the Tafel slope. MUSCP was executed using a constant current density of 0.5 to 3 mA cm^{-2} at incremental steps of 0.5 mA cm^{-2}. Long-term CP testing for 24 hours was performed at a current density of 10 mA cm^{-2} using 2.5 mg of precatalyst dissolved in 0.2 wt% Nafion® perfluorinated resin solution (dissolved in isopropanol) (Sigma Aldrich).

Faradaic efficiency measurements

Faradaic efficiency was measured using a Hoffman cell in which one of the arms serves as the collection point for the hydrogen evolution reaction (HER) and the other for the OER. The HER side was catalyzed by a standard Pt/C electrode, while the OER side was catalyzed by the precatalysts of interest, which are Ce_0Ni_1-NMOF and $Ce_{0.03}Ni_{0.97}$-NMOF drop-cast on carbon paper. The Hoffman cell was appropriately filled with 1 M KOH; the HER side of the cell served as the counter electrode, while the OER side holding the tested precatalyst served as the working electrode. On the CH instrument software, the chronopotentiometry experiment was performed and the software settings applied were as follows: the cathodic current applied is 0 mA, the time for cathodic current was 0 s, the anodic current was 10 mA, and time for anodic current was 6 hours. The potential limit was set at ±5 V, and the current switching priority was time-dependent. The current, time of charge flow, and volume of the gas obtained from the experiment were used in the equation, $f = 4Fn/Q$ to calculate the faradaic efficiency, where f is the faradaic efficiency (%), F is the Faraday constant (96 485 C mol^{-1}), n is the amount (mol) of O_2 gas evolved, and Q is the total charge passed during electrolysis.

In situ Raman measurements

The *in situ* Raman measurements were obtained using two different lasers. The first setup involved drop-casting 24 μL (3 μL × 8) on a gold substrate, which was assembled in a 3D-printed cell[45,46] using 1 M KOH electrolyte, and the reference and counter electrodes were Hg/HgO (1 M KOH) and graphite, respectively. A Renishaw inVia Raman system, comprising an Ar-ion laser (514 nm, 50 mW), supplied an excitation beam, which was focused onto the sample *via* a 50× objective lens microscope. The laser was stationed above the working electrode and covered with a polymer film to avoid contact with the electrolyte. The spectro-electrochemistry sequence was obtained in the spectrum range between 200 and 2000 cm^{-1}, and the laser exposure time was 30 s. First, the spectroelectrochemistry was obtained at the open circuit potential, and subsequent electrochemistry was simultaneously obtained using chronoamperometry at potentials between 1.0 and 1.6 V *vs.* RHE for the same period.

In the second setup, a gold screen-printed electrode (SPE) was electrochemically roughened by covering the surface of the working electrode with 0.1 M KCl (~100 μL) followed by thirty CV scans. The *in situ* surface-enhanced Raman (SERS) measurements were performed by drop-casting 5 μL (1 μL × 5) of the precatalyst on the Au SPE which was assembled in a 3D-printed cell using 1 M KOH electrolyte, and the reference and counter electrodes were Hg/HgO (1 M KOH) and nickel foam (2 × 2 cm^2), respectively.[47] A Horiba LabRAM ARAMIS confocal Raman microscope system, comprising a He–Ne laser (633 nm, 50 mW) supplied an excitation beam focused on the sample *via* a 50× objective lens microscope. The laser was stationed above the electrochemical cell with a polymer film window to avoid contact with the electrolyte. The spectro-electrochemistry sequence was obtained in the spectrum range between 200 and 2000 cm^{-1} and the laser exposure time was 30 s. First, the spectro electrochemistry was obtained at the open circuit potential, and subsequent electrochemistry was simultaneously obtained using chronoamperometry at potentials between 1.0 and 1.6 V *vs.* RHE for the same period.

ICP-MS measurements

The variants of the Ce_xNi_{1-x}-NMOF were digested by first weighing 2.5 mg of the samples and dissolving them in 1 mL of aqua regia. The samples were digested and heated to dryness at 108 °C for 1 hour using a 5 mL conical interior Savillex vial, after which the samples were allowed to cool. After drying, the samples were reconstituted with 3 mL of aqua regia. All samples were diluted 37.5-fold using 2% HNO_3 by mixing 267 μL of the samples in a total volume of 10 mL of 2% HNO_3 for two reasons:

To keep the total dissolved solids below 200 ppm is a required safety precaution for the instrument.

To eliminate the matrix effect that may occur due to density differences between the digesting solvent (aqua regia) and the calibration solvent (2% HNO_3).

Next, the samples were diluted further to keep Ce at concentrations <200 ppb, which is the maximum calibration

standard used for rare earth metals. This was completed by dissolving 15 μL of the previous diluent in 10 mL of 2% HNO_3.

Microcrystal electron diffraction (MicroED)

Microcrystal electron diffraction (MicroED) data were collected as described by Jones *et al.*[48] Powders of Ce_0Ni_1-NMOF and $Ce_{0.03}Ni_{0.97}$-NMOF were ground lightly between glass microscope slides and transferred to carbon–copper TEM grids. Diffraction data were measured using a ThermoFisher Glacios cryogenic transmission electron microscope (TEM) at a temperature of 100 K and an accelerating voltage of 200 kV (0.0251 Å). The sample stage was continuously rotated from −60° to +60° at a rate of 1° s^{-1} and data were collected using EPU-D data collection software; patterns were recorded on a Ceta-D camera optimized for low-dose diffraction. Crystals suitable for diffraction were sparse, and only one crystal from each sample batch yielded diffraction data suitable for indexing and subsequent structure solution. For Ce_0Ni_1-NMOF, this crystal diffracted to 0.65 Å and for $Ce_{0.03}Ni_{0.97}$-NMOF the crystal diffracted to 0.70 Å. Despite the low symmetry and incompleteness of the data, the relatively high resolution made structure solution possible.

Data reduction was performed using X-ray Detector Software (XDS).[49] Using Olex2 1.5,[50] the structure was solved *via* intrinsic phasing using SHELXT and refined by full-matrix least-squares on F^2 with anisotropic displacement parameters for the non-H atoms using the SHELXL[51] refinement package utilizing electron scattering factors.[52] Hydrogens were inserted using the HADD function and refined isotropically in idealized positions. The refinement of the occupancies of the O and N positions was guided by FTIR data collected from the samples. The occupancies were refined at $\frac{1}{2}$ for N and O atoms in the Ce_0Ni_1-NMOF; while in the $Ce_{0.03}Ni_{0.97}$-NMOF, the occupancy of O was $\frac{3}{4}$ and the occupancy of N was 1.4. Restraints (RIGU 0.001, ISOR 0.005) on anisotropic displacement parameters were necessary. Details of crystal data, data collection, and structure refinement are listed in Table S2.

Results and discussion

Nitridation temperature optimization

The nickel-MOF (Ce_0Ni_1-MOF) was nitrided into Ce_xNi_{1-x}-NMOF employing a series of temperatures from 300–450 °C under NH_3 flow to obtain the optimum temperature needed for the formation of the Ni_3N phase. As shown in Fig. S1,

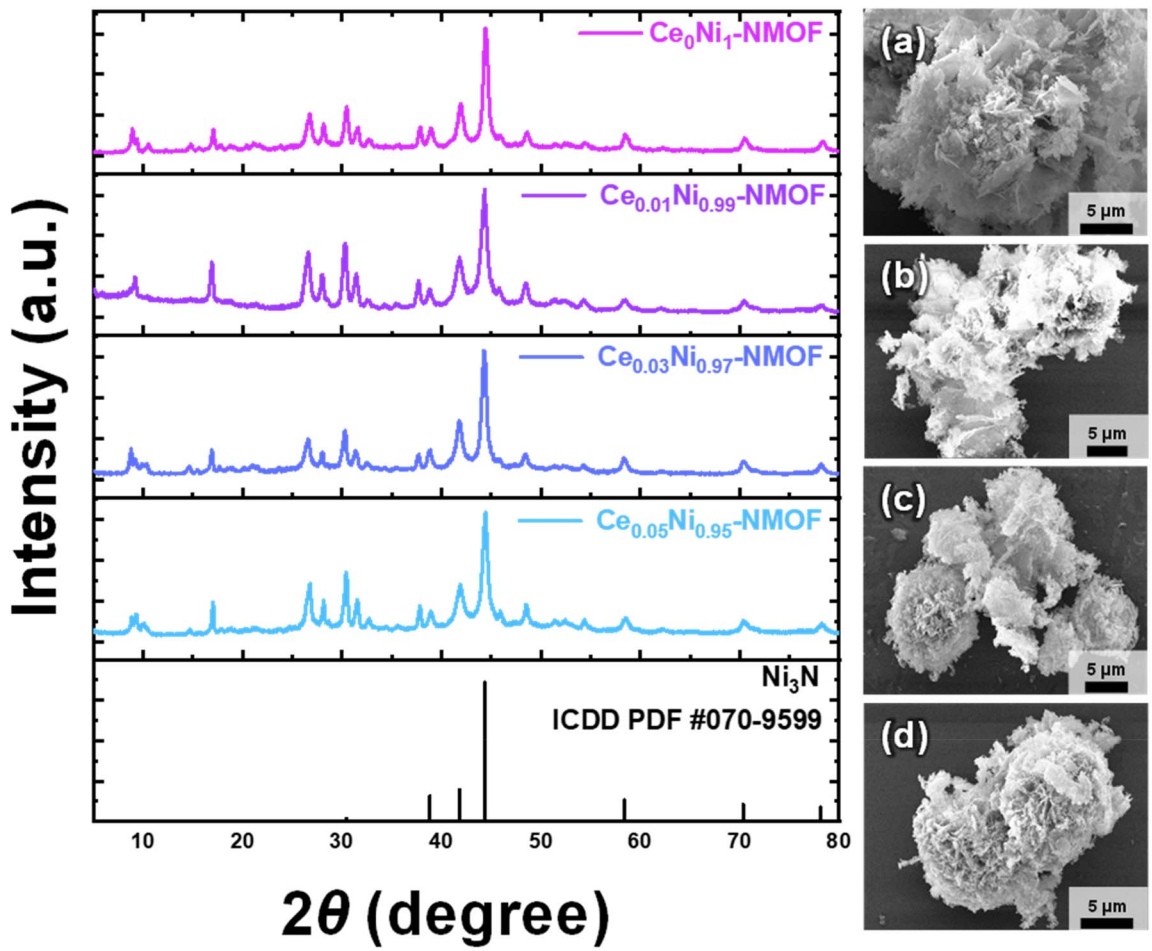

Fig. 1 XRD and SEM images of pristine (a) Ce_0Ni_1-NMOF, (b) $Ce_{0.01}Ni_{0.99}$-NMOF, (c) $Ce_{0.03}Ni_{0.97}$-NMOF, and (d) $Ce_{0.05}Ni_{0.95}$-NMOFs. Ce-doping does not impact the bulk composite crystal and morphology.

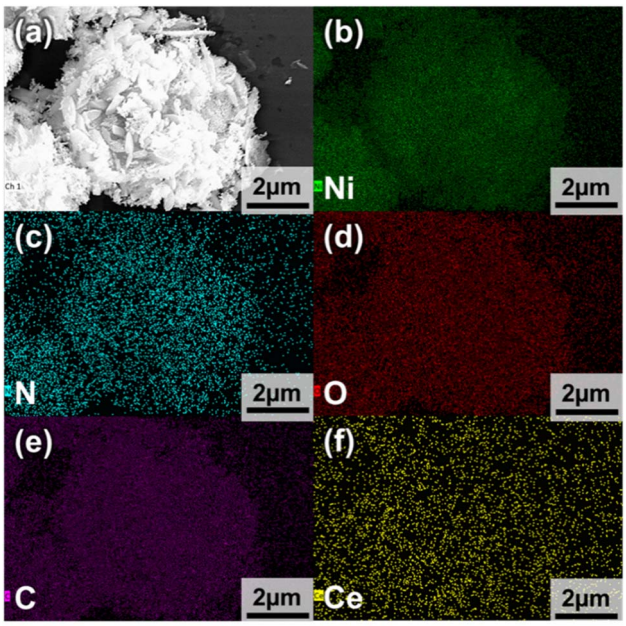

Fig. 2 SEM and EDX elemental mapping images of $Ce_{0.03}Ni_{0.97}$-NMOFs. (a) Flower-like morphology (b) nickel (c) nitrogen (d) oxygen (e) carbon (f) cerium.

temperatures above 350 °C resulted in metallic nickel with possibly reconstructed carbon fragments from the MOF as the dominant phase, which is due to excessive reduction. However, at 350 °C, the diffraction patterns match the formation of nickel nitride and a reconstructed carbon framework. This suggests that 350 °C is the optimum temperature needed for the desirable formation of the nitride phase.

Precursor to precatalyst characterization

The Ce_xNi_{1-x}MOFs and Ce_xNi_{1-x}NMOFs were characterized by powder X-ray diffraction (PXRD) to obtain crystallographic information about the samples. As displayed in Fig. S2, all the samples shared diffraction patterns similar to those of the parent MOF-Ce_0Ni_1MOF (CCDC #638866),[43] which meant that Ce-doping didn't change the crystal structure, and this is very likely due to the low concentration. Upon nitridation of the Ce_xNi_{1-x}MOFs, the as-obtained Ce_xNi_{1-x}NMOF diffraction patterns, as shown in Fig. 1, were all similar; hence it can be inferred that the bulk of the sample was not impacted by Ce-doping even after nitridation. Next, we evaluated the morphology and chemical composition of the Ce_xNi_{1-x}NMOFs using SEM and EDX. SEM images in Fig. 1 and S3–S5 reveal that all Ce_xNi_{1-x}-NMOFs exhibited a flower-like architecture with a mixed crystalline–amorphous and sheet-like morphology (see also in Fig. S23). EDX elemental mapping in Fig. 2 and S3–S5 shows a homogenous distribution of the elements with a sparse distribution of cerium in the bulk, as expected. Their corresponding EDX spectra in Fig. S6 and S7 also indicate the presence of the constituent elements in the bulk of all Ce_xNi_{1-x}-NMOFs samples.

Next, we examined the Ce_xNi_{1-x}MOFs and the Ce_xNi_{1-x}-NMOFs using X-ray photoelectron spectroscopy (XPS) to

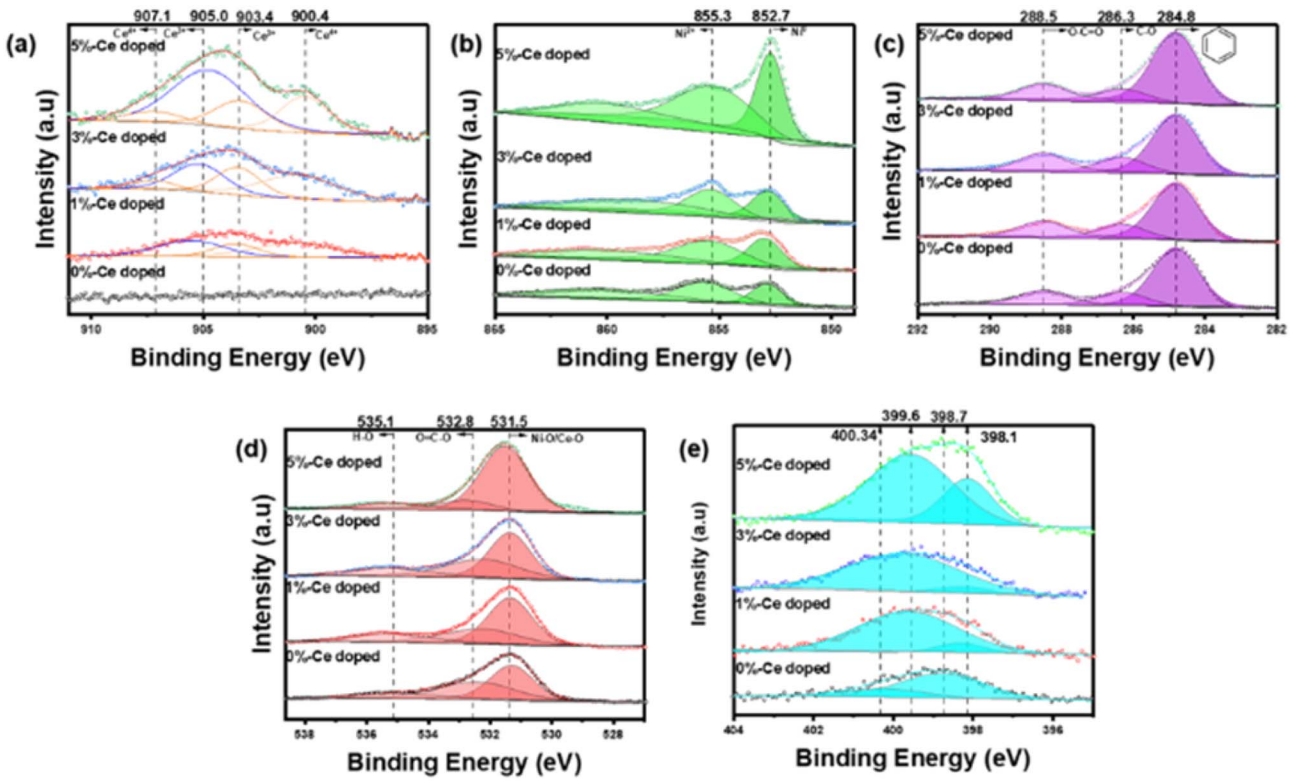

Fig. 3 XPS spectra of Ce_xNi_{1-x}-NMOFs showing (a) Ce 3d, (b) Ni 2p, (c) C 1s, (d) O 1 s, and (e) N 1s.

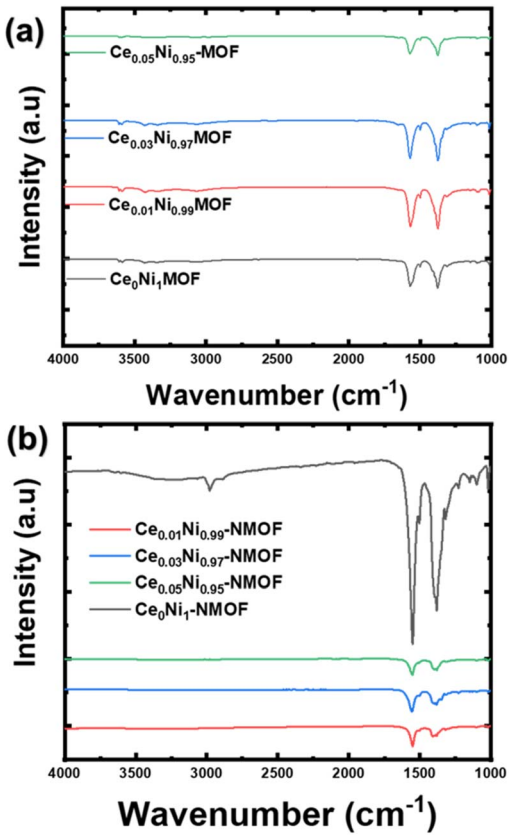

Fig. 4 FTIR spectra showing functional group vibrational bands in (a) Ce_xNi_{1-x}-MOF and (b) Ce_xNi_{1-x}-NMOF.

determine the chemical speciation on the surface. High-resolution spectra in Fig. S9 show that the pristine Ce_xNi_{1-x}-MOFs comprise Ce 3d, Ni 2p, O 1s, and C 1s core levels on the surface. All the elements in the sample sets were charge-corrected with a C 1s value of 284.8 eV. In Fig. S9a, the peaks between 898 and 910 eV are due to Ce $3d_{3/2}$ spin–orbit coupling, and they show that Ce exists predominantly as Ce^{3+} species (904.0 eV) with Ce^{4+} species (899.9 and 906.7 eV) occurring due to surface oxidation.[53–55] In Fig. 3a, although the Ce_xNi_{1-x}-NMOFs showed an increased mixture of Ce^{4+} and Ce^{3+} species with Ce-doping, there is an increase in the Ce^{3+} population compared to that of Ce_xNi_{1-x}MOFs which can be attributed to the reduction of Ce^{4+} species under a reducing ammonia atmosphere. The reduction starts with the thermal dissociation of ammonia into H_2 and NH_x radical ions, which interact with Ce^{4+} to release or extract oxygen, leading to the formation of oxygen vacancies and the byproduct Ce^{3+}.[56]

The Ni $2p_{3/2}$ band for Ce_xNi_{1-x}MOFs (Fig. S9b) shows that Ni^{2+} (855.9 and 859.4 eV) species exist as Ni–O and Ni–OH which are the bonding environments between Ni and terephthalic acid (TPA).[57] The intensity of the Ni^{2+} peaks decreased and the binding energy shifted slightly to the right with increasing Ce content. In addition, the Ce^{3+} to $Ni^{>2+}$ charge transfer is evident from the increase in the Ce^{4+} population as confirmed in the Ce 3d spectra (see Fig. S9a). Upon nitridation, the Ni band in Fig. 3b indicates a binding energy shift to 852.6 from 855.0 eV (in Fig. S9b), indicating the formation of Ni^0, which is direct evidence for the formation of the metallic nickel nitride phase,[58–60] corroborating the diffraction pattern in Fig. 1. C 1s spectra in Fig. 3c indicate the presence of the benzoic ring, carbonyl, and C–O groups from the TPA linkers at 284.8, 288.5, and 286.3 eV, respectively.[57] Core level spectra for O 1s in Fig. 3d show a mix of Ni and Ce lattice hydroxides at 531.4, while 532.4 and 535.1 eV represent oxygen from the carbonyl groups and adsorbed water, respectively.[57,61] In Fig. 3e, the N 1s spectra for all Ce_xNi_{1-x}NMOFs are shown. The binding energies at 398.1 eV and 399.6 eV indicate the presence of the lattice Ni–N bond,[58–60] and adsorbed NH_2 (ref. 62), respectively, for all the nitrided Ce-doped samples (black arrows). Ce_0Ni_1-NMOFs exhibited an oxidized surface chemistry as indicated by a shift in the binding energy from 398.1 eV (Ce-doped) to 398.7 eV and the adsorption of NH_x species at 400.3 eV.[58–60] These results indicate that nitirdation aids the formation of metallic nickel nitride.

Next, Ce_xNi_{1-x}MOFs and Ce_xNi_{1-x}NMOFs were characterized with FTIR to determine the functional group distribution in the samples. In the group frequency region as shown in Fig. 4a, 1570 and 1375 cm^{-1} represent coordinated bi-dentate vibrations modes from v_{asym}(COO) and v_{sym}(COO) respectively from the TPA linker.[63–66] Additional vibrational modes between 3058 and 3427 cm^{-1} can be ascribed to strong OH stretching from adsorbed water while bands between 3587 and 3608 cm^{-1} indicate the presence of weak OH– stretching perhaps from remnant ethanol used in the washing process.[67,68] After nitridation, the as-synthesized Ce_xNi_{1-x}-NMOF spectra in Fig. 4b show that all the samples exhibited a red shift for v_{asym}(COO) from 1570 to 1556.46 cm^{-1} which can be attributed to attenuation or removal of some v_{asym}(COO) bonds within the molecule by volatilization as CO_2 (g) or stronger coordination of v_{asym}(-COO) to Ni centers. Conversely, v_{sym}(COO) exhibited a blue shift from 1375 to 1382 cm^{-1} which can be attributed to two factors. First, the availability of free v_{sym}(COO) due to the weakening or replacement of some of the v_{sym}(COO) coordinated to the Ni center with the Ni–N bond (not observed in IR). In addition, this can also be attributed to the coordination switch of v_{sym}(COO) from Ce to Ni after nitridation for the Ce-containing samples.

Intrinsic OER activity

The electrochemical performance of the various precatalysts was evaluated to check the effect of Ce-doping and nitridation. To understand the role of Ce-doping in electrocatalytic performance, the OER geometric activity was measured using CV as shown in Fig. 5a. The results in Fig. 5b indicate that the overpotentials of Ce_0Ni_1-NMOF, $Ce_{0.01}Ni_{0.99}$-NMOF, $Ce_{0.03}Ni_{0.97}$-NMOF, and $Ce_{0.05}Ni_{0.95}$-NMOF are 527 ± 31.64, 465 ± 16.80, 426 ± 12, and 528 ± 29.64 mV, respectively with $Ce_{0.03}Ni_{0.97}$-NMOF showing the lowest value. The Tafel slope was measured using steady-state multi-step chronopotentiometry (MUSCP) as indicated in Fig. S10, and representative resultant Tafel plots are shown in Fig. S11, while results from replicate measurements are also available in Fig. 5b. The results demonstrate that the Tafel slope values were 114.32 ± 4.67, 97.74 ± 1.45, 83.6 ± 7.19, and 95.87 ± 3.33 mV dec^{-1} for Ce_0Ni_1-NMOF, $Ce_{0.01}Ni_{0.99}$-

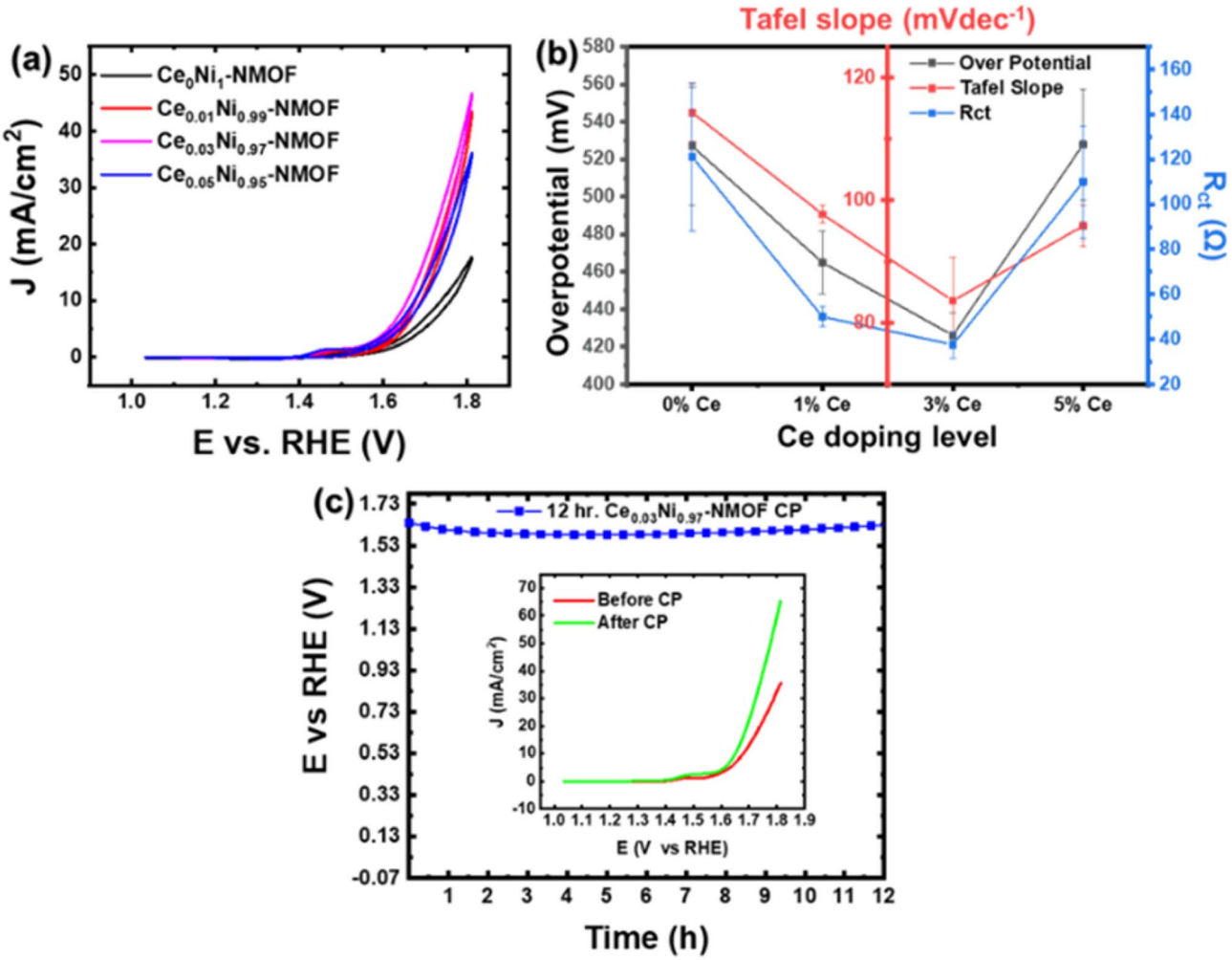

Fig. 5 (a) CV showing the impact of Ce doping on electrochemical activity. (b) Effect of Ce-doping on electrochemical metrics. (c) CP plot showing electrochemical stability of $Ce_{0.03}Ni_{0.97}$-NMOF with the inset showing linear sweep voltammetry curves indicating activity.

NMOF, $Ce_{0.03}Ni_{0.97}$-NMOF, and $Ce_{0.05}Ni_{0.95}$-NMOF, respectively. A similar trend was observed in the R_{ct} values measured using EIS (Fig. S12, results in Fig. 5b), where $Ce_{0.03}Ni_{0.97}$-NMOF has the lowest value of $37.6 \pm 5.82\ \Omega$. Clearly, the $Ce_{0.03}Ni_{0.97}$-NMOF had a better electrochemical performance compared to others. Catalytic performance was also assessed by measuring the double-layer capacitance (C_{dl}) using EIS and then normalizing to a generic specific capacitance (C_s) of 40 μF cm^{-2} in an alkaline system to obtain the electrochemical surface area (ECSA).[69] The results in Fig. S13a reveal that the $Ce_{0.03}Ni_{0.97}$-NMOF has one of the lowest ECSAs and the highest intrinsic activity as indicated by the current density normalized to the ECSA in Fig. S13b. However, it was observed that at cerium concentrations >3%, the population of ceria (Ce^{4+}), which is a well-known insulator, accumulates on the surface as observed in Fig. 3a and could likely increase under oxidizing reaction conditions. Next, we tried to evaluate the stability of the $Ce_{0.03}Ni_{0.97}$-NMOF using long-term CP, and the result shown in Fig. 5c shows that the electrocatalyst is stable for at least 12 hours at a current density of 10 mA cm^{-2}. The observed decrease in potential could be due to increasingly exposed active sites under prolonged OER conditions, which lowered the energy requirement for the OER. It's also noteworthy that the electrochemical activity (inset of Fig. 5c) increases by ~25 mA cm^{-2} after long-term CP testing, demonstrating that the electrochemical performance improves even after 12 hours. We also conducted a 24 hour CP test, as shown in Fig. S22, and $Ce_{0.03}Ni_{0.97}$-NMOF still maintains its stability. Post-long-term CP characterization by EDX, shown in Fig. 6 (spectra in Fig. S8a), shows that $Ce_{0.03}Ni_{0.97}$-NMOF retains its Ni and O content. However, the C and N signals are convoluted with signals emerging from the carbon paper and the fumion ® binder, respectively. XPS spectra (shown in Fig. S8b) reveal that the N 1s peak at 398.1 eV diminishes significantly compared to the pristine $Ce_{0.03}Ni_{0.97}$-NMOF, which is an indication of the loss of lattice nitrogen.[59] In addition, the peak at ~403.5 eV, which was absent in the pristine sample, becomes prominent, which can be attributed to nitrogen contributions from the Fumion® binder. Pristine and post-OER electrolyte analysis (Table S1) using ICP-MS showed that Ce was not present in the electrolyte before the reaction, nor was there any leaching of Ce from $Ce_{0.03}Ni_{0.97}$-NMOF which is also an indication of its electrochemical stability.

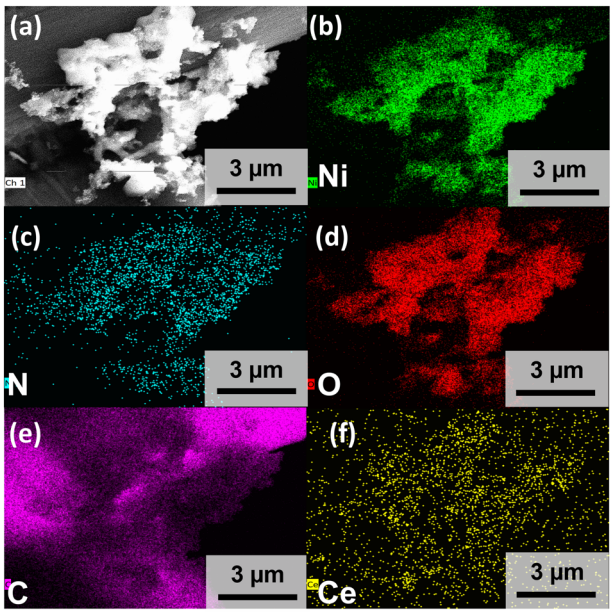

Fig. 6 Post-OER SEM and EDX elemental mapping images of the $Ce_{0.03}Ni_{0.97}$-NMOF.

To evaluate the kinetic regime governing $Ce_{0.03}Ni_{0.97}$-NMOF, a scan-rate dependent electrochemical analysis was conducted to probe mass transport behavior. CVs were recorded at varying scan rates, and the relationship between peak current and scan rate was analyzed using the power-law expression ($i = av^b$).[70] A b-value of 0.74 was obtained. In electrochemical systems, a b-value of 0.5 corresponds to a diffusion-controlled process, whereas a value approaching 1.0 indicates a surface-controlled or capacitive process. The observed intermediate b-value of 0.74 suggests that the catalytic response is governed by a mixed mechanism, with contributions from both diffusion-limited mass transport and surface or pseudocapacitive charge-transfer processes.[70,71] This indicates that although ion diffusion within the electrolyte and porous catalyst framework influences the overall current response, a substantial fraction of the current originates from rapid interfacial redox reactions occurring at accessible active sites. Overall, the results demonstrate partial mitigation of diffusion limitations and enhanced surface reactivity, consistent with improved electrochemical performance.

Next, to show that nitridation played an active role in the OER activity, we compared the electrochemical activity of the best-performing precatalyst $Ce_{0.03}Ni_{0.97}$-NMOF with its MOF counterpart, $Ce_{0.03}Ni_{0.97}$-MOF. As shown in Fig. S14, nitrogen incorporation into the lattice structure of the MOF improved its electrochemical activity by approximately a factor of 50. This re-emphasizes the role of nitrogen incorporation into the crystal lattice of MOFs in augmenting electron transfer, thereby aiding electrochemical activity.[72]

Structural contributions to improved OER activity

With PXRD unable to discern between the Ce-doped and undoped nitride samples, in the next step, we employed the more precise microcrystal electron diffraction (MicroED) method to obtain the structure of the synthesized Ce_xNi_{1-x}-NMOF and delineate a structural explanation for the electrochemical activity. MicroED is uniquely beneficial for the structural interrogation of micro-crystalline samples in the absence of large crystals required for conventional single-crystal XRD analysis. The crystal structure solved by MicroED (Fig. S15a) shows that the Ce_0Ni_1-NMOF possesses a linear or 1D structure. It does not contain Ce as expected, and Ni resides in a pseudo-octahedral sphere coordinated with oxygen atoms from the benzoic acid functionality of TPA, in accordance with FTIR results. The nitrogen atoms are also observed to be bonded to the Ni atom in the chemical structure of Ce_0Ni_1-NMOF which supports the XRD results. Surprisingly, the crystal structure of $Ce_{0.03}Ni_{0.97}$-NMOF (Fig. S15b) does not indicate the presence of Ce. The absence of Ce in $Ce_{0.03}Ni_{0.97}$-NMOF could be due to its absence in the bulk due to its low concentration which makes it below the detection limit of MicroED. However, because the cerium content is on the surface, rather than in the bulk, it can be detected with XPS. Also, Ce exists in an amorphous phase, which is also a condition under which MicroED cannot resolve structures. The Ni atoms exist in unique pseudo-octahedral and pseudo-tetrahedral geometries, coordinated by oxygen atoms from TPA as predicted by FTIR or by nitrogen atoms as predicted by XRD. Oxygen is resolved to possess 75% occupancy due to its predominant fingerprint in other characterization techniques such as XPS and FTIR while nitrogen is resolved to have 25% occupancy since C=N or C–N bonds weren't observed in FTIR perhaps due to their lower abundance. The pseudo-tetrahedral geometry of Ni (as opposed to the octahedral geometry) can be ascribed to oxygen removal by cerium doping.

The chemical structure of $Ce_{0.03}Ni_{0.97}$-NMOF suggests that the pseudo-tetrahedral geometry at Ni leaves room for the adsorption of OH* adsorbates thereby facilitating OER compared to Ce_0Ni_1-NMOF.[7,39–42] It is well reported that Ce has a high affinity for oxygen atoms, as indicated by a higher bond dissociation energy of 795 kJ mol^{-1} compared to Ni (391 kJ mol^{-1}),[73] and this may lead to structural evolution near Ni.[74] It is also possible that Ce-doping disrupts the neighboring Ni–O bond formation and, coupled with carboxylate recoupling leads to the growth of $Ce_{0.03}Ni_{0.97}$-NMOF in a periodic 3D lattice. To provide evidence for the location/presence of Ce and nitride species in the precatalyst, we obtained TEM images and elemental mapping. Elemental mapping of Ce_0Ni_1-NMOF in Fig. S16 shows the spatial distribution of the expected elements, most importantly nitrogen confirming the presence of nitride species, which is supported by the corresponding spectra in Fig. S18a indicating the clear absence of Ce and the detection of nitrogen as expected. The presence of Ce and nitrogen in $Ce_{0.03}Ni_{0.97}$-NMOF is also confirmed by the elemental mapping shown in Fig. S17 which is supported by the spectra in Fig. S18b. Nonetheless, ICP-MS further confirmed the presence of Ce in the various Ce-doped samples and verified that the Ce : Ni ratio is as synthesized, as shown in Table S1.

In situ Raman measurements were performed to observe characteristic vibration modes of the active phases during key OER events and potentials for Ce_0Ni_1-NMOF and $Ce_{0.03}Ni_{0.97}$-

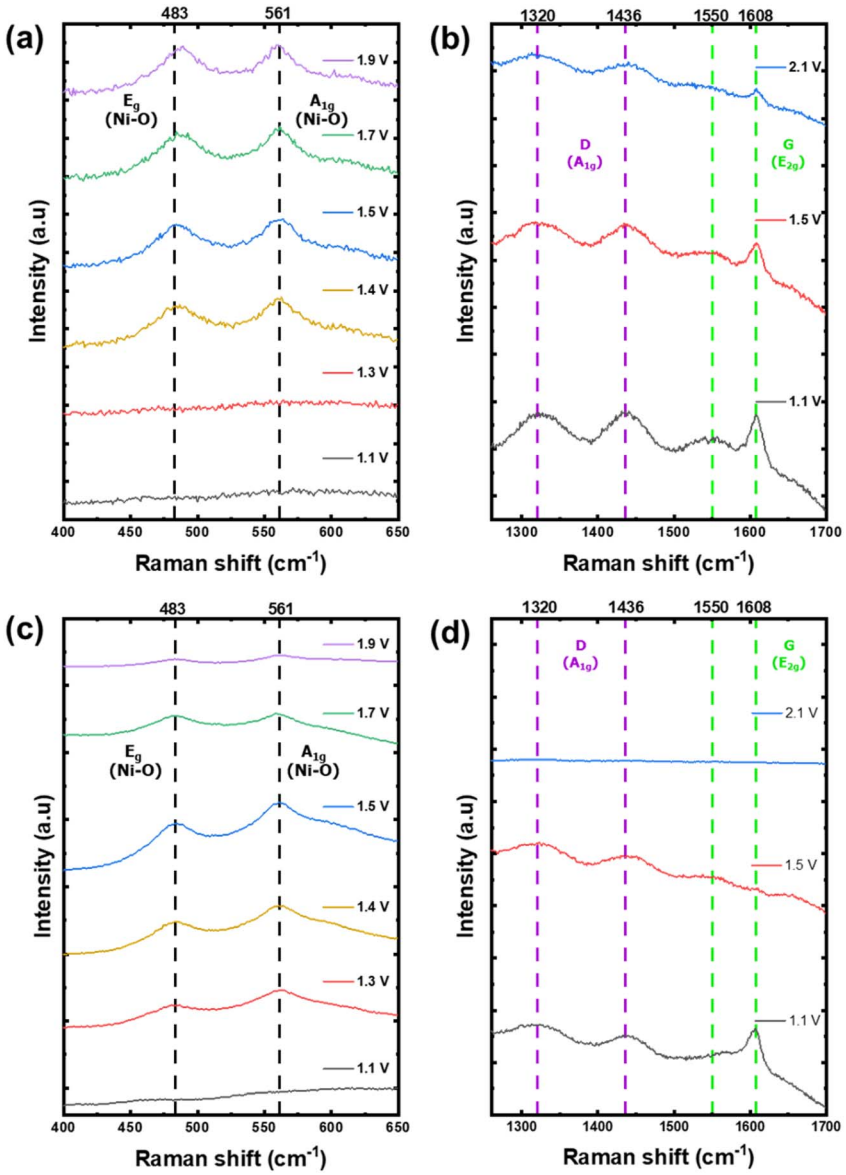

Fig. 7 *In situ* surface-enhanced Raman measurements (633 nm) at various potentials showing (a) NiOOH and (b) graphitic carbon bands in Ce_0Ni_1-NMOF and (c) NiOOH and (d) graphitic carbon bands in $Ce_{0.03}Ni_{0.97}$-NMOF.

NMOF. This was done to identify the catalytic OER active phases and provide further insight into the role of Ce-doping during the OER. As shown in Fig. 7a, at potentials ≤1.3 V *vs.* RHE, Raman bands of Ce_0Ni_1-NMOF at 483 and 561 cm^{-1} which correspond to Ni–O vibrations in NiOOH (ref. 75 and 76) were absent, while in Fig. 7b, peaks at 1320–1436 and 1550–1608 cm^{-1}, were observed which are indicative of the D (A_{1g} mode) and G (E_{2g} mode) graphitic carbon bands, respectively.[77,78] This suggests that prior to OER onset potentials (≤1.3 V *vs.* RHE), the graphitic carbon frameworks are present, which has been confirmed by other characterization techniques; and the nickel-nitride sites are yet to be oxidized sufficiently to generate the Ni–O bond in NiOOH. In addition, since the D band typically represents defects in a carbon framework while the G bands represent sp^2 in-plane vibrational modes, the relatively smaller intensity of the G-band compared to the D-band provides evidence that there are more structural defects in the carbon framework than an ordered carbon ring structure below OER potentials.[79] However, at OER overpotentials, specifically 1.40 V *vs.* RHE, the twin Ni^{3+}–O modes at 483 and 561 cm^{-1} are observed, indicating the oxidation of Ni_3N to NiOOH. Previous studies have shown that Raman shifts at 483 and 561 cm^{-1} correspond to theβ-NiOOH phase.[80] In addition, as the potentials increase from 1.1 to 2.1 V *vs.* RHE, there is a gradual diminishing of the carbon bands. Two possible reasons for the peak disappearance could be OER conditions or the beam energy.[81,82] To determine which of the aforementioned reasons is dominant, we interrogated the surface in an *ex situ* setup. After the *ex situ* interrogation of the precatalyst, the emergence of the graphitic framework was observed as shown in Fig. S19. The resulting evidence suggests that some of the graphitic carbon structure was preserved even after the OER,

and the absence of the graphitic carbon framework can be due to beam damage due to prolonged exposure. Another experiment was conducted with a high energy beam of 514 nm and as shown in Fig. S20a and b, the Ni–O peaks at 477–560 cm^{-1} and the carbon bands at 1381–1606 cm^{-1} were diminished indicating the role of beam intensity in the observed Raman features. In Fig. 7c and d, a similar observation in Ce_0Ni_1-NMOF is noted for the $Ce_{0.03}Ni_{0.97}$-NMOF Raman bands. Unlike Ce_0Ni_1-NMOF, an early development of the β-NiOOH peak at 1.3 V is observed for the $Ce_{0.03}Ni_{0.97}$-NMOF that wasn't observed in Ce_0Ni_1-NMOF which suggests that incorporation of Ce induces the early formation of the active site that facilitates OER activity by generating highly active CeO_2–NiOOH due to the formation of the pseudo-tetrahedral structure as suggested by MicroED. At potentials ≥1.3 V *vs.* RHE, where OER currents are observed, the twin peaks of β-NiOOH emerge as the dominant active sites in that regime. Also, the graphitic carbon framework completely disappears as observed in Fig. 7d at 2.1 V, but is observed even in the *ex situ* setup after the OER (Fig. S19) with the D bands having higher intensity compared to the pristine material, indicative of increased disorder in the graphitic carbon framework. The faster decrease in the intensity of the carbon bands in $Ce_{0.03}Ni_{0.97}$-NMOF compared to Ce_0Ni_1-NMOF in the *in situ* setup may additionally be due to the higher activity of the former compared to the latter.

Conclusions

We outlined a synthetic method that utilizes nitridation and Ce-doping to transform a non-conductive Ni-based MOF into a conductive precatalyst suitable for driving the OER in alkaline media. Nitridation modified the chemical environment and electronic properties of the parent MOF while Ce-doping possibly aided the formation of pseudo-tetrahedral geometry at Ni sites which likely impacted the binding energy of the adsorbates leading to improved intrinsic activity. By applying different temperature regimes, we optimized the nitridation process which yielded metallic Ni^0 and Ce^{3+} as the metallic centers and a flower-like carbon framework. Electrochemical data reveal that among the various Ce-doped precatalysts, $Ce_{0.03}Ni_{0.97}$-NMOF had the best OER performance as indicated by the highest intrinsic activity, lowest charge transfer resistance, and Tafel slope. Further evaluation revealed that $Ce_{0.03}Ni_{0.97}$-NMOF was stable for 12 hours at a current density of 10 mA cm^{-2} and even demonstrated improved electrochemical activity afterward. With MicroED, the pseudo-tetrahedral geometry at Ni sites was structurally observed, and *in situ* Raman measurement revealed that this geometry induces early formation of β-NiOOH, which is also an OER active phase responsible for improved electrochemical metrics. Overall, the results show that nitridation and Ce-doping produced a precatalyst with augmented activity and stability relative to the parent Ni-based MOF.

Author contributions

C. E. Chukwuneke: conceptualization, investigation, methodology, formal analysis, writing – original draft, visualization. K. Kawashima: conceptualization, investigation, methodology, formal analysis, writing – review and editing, visualization. T. P. A Nguyen: investigation. G. Ruiz: investigation, writing, formal analysis. JP. Smith: investigation. R. A. Márquez: investigation, writing – review & editing. J. T. Bender: investigation, writing – review & editing. X. Zhan: investigation. D. J. Milliron: writing – review & editing, resources. M. J. Rose: writing – review & editing, resources. C. B. Mullins: writing – review & editing, resources, funding acquisition, project administration.

Conflicts of interest

There are no conflicts to declare.

Data availability

All data are available in the manuscript and supplementary information (SI) files. Supplementary information is available. See DOI: https://doi.org/10.1039/d5ta09289b.

Acknowledgements

The authors gratefully acknowledge the support of the National Science Foundation (NSF) *via* Grant CHE-2102307 and the acquisition of the VersaProbe-IV XPS supported by the NSF Major Research Instrumentation program (Grant MRI-2117623). This project was also supported by the Allen J. Bard Center for Electrochemistry through the Welch Grant "Welch Foundation H-F-0037", grants supporting MJR/GNR "Welch Foundation grants F-1822 and X-F-0003-20230731", and Welch grant number F-1848. MicroED data were collected at the Sauer Structural Biology Laboratory at the University of Texas at Austin.

References

1 N. Stock and S. Biswas, *Chem. Rev.*, 2012, **112**, 933–969.
2 A. Mahmood, W. Guo, H. Tabassum and R. Zou, *Adv. Energy Mater.*, 2016, **6**, 1600423.
3 W. Zheng and L. Y. S. Lee, *ACS Energy Lett.*, 2021, **6**, 2838–2843.
4 W. Zheng, M. Liu and L. Y. S. Lee, *ACS Catal.*, 2020, **10**, 81–92.
5 K. Kawashima, R. A. Márquez, L. A. Smith, R. R. Vaidyula, O. A. Carrasco-Jaim, Z. Wang, Y. J. Son, C. L. Cao and C. B. Mullins, *Chem. Rev.*, 2023, **123**, 12795–13208.
6 O. Mabayoje, A. Shoola, B. R. Wygant and C. B. Mullins, *ACS Energy Lett.*, 2016, **1**, 195–201.
7 B. R. Wygant, K. Kawashima and C. B. Mullins, *ACS Energy Lett.*, 2018, **3**, 2956–2966.
8 S. Jin, *ACS Energy Lett.*, 2019, **4**, 1443–1445.
9 Y. Li, B. Jia, Y. Fan, K. Zhu, G. Li and C.-Y. Su, *Adv. Energy Mater.*, 2018, **8**, 1702048.
10 T. Wang, Z. Kou, S. Mu, J. Liu, D. He, I. S. Amiinu, W. Meng, K. Zhou, Z. Luo, S. Chaemchuen and F. Verpoort, *Adv. Funct. Mater.*, 2018, **28**, 1705048.

11 Z. Wang, Y. Lu, Y. Yan, T. Y. P. Larissa, X. Zhang, D. Wuu, H. Zhang, Y. Yang and X. Wang, *Nano Energy*, 2016, **30**, 368–378.
12 B. Y. Xia, Y. Yan, N. Li, H. B. Wu, X. W. Lou and X. Wang, *Nat. Energy*, 2016, **1**, 1–8.
13 F. Yang, P. Zhao, X. Hua, W. Luo, G. Cheng, W. Xing and S. Chen, *J. Mater. Chem. A*, 2016, **4**, 16057–16063.
14 Y.-N. Chen, Y. Guo, H. Cui, Z. Xie, X. Zhang, J. Wei and Z. Zhou, *J. Mater. Chem. A*, 2018, **6**, 9716–9722.
15 B. Chen, X. He, F. Yin, H. Wang, D.-J. Liu, R. Shi, J. Chen and H. Yin, *Adv. Funct. Mater.*, 2017, **27**, 1700795.
16 L. Wei, H. E. Karahan, S. Zhai, H. Liu, X. Chen, Z. Zhou, Y. Lei, Z. Liu and Y. Chen, *Adv. Mater.*, 2017, **29**, 1701410.
17 J. Qian, T.-T. Li, Y. Hu and S. Huang, *Chem. Commun.*, 2017, **53**, 13027–13030.
18 J. Jiang, C. Zhang and L. Ai, *Electrochim. Acta*, 2016, **208**, 17–24.
19 X. Dong, E. Yan, Y. Lv, Y. Zhou and X. Chu, *Appl. Catal., A*, 2024, **681**, 119772.
20 S. Anantharaj, S. R. Ede, K. Sakthikumar, K. Karthick, S. Mishra and S. Kundu, *ACS Catal.*, 2016, **6**, 8069–8097.
21 F. Ming, H. Liang, H. Shi, X. Xu, G. Mei and Z. Wang, *J. Mater. Chem. A*, 2016, **4**, 15148–15155.
22 S. Li, S. Peng, L. Huang, X. Cui, A. M. Al-Enizi and G. Zheng, *ACS Appl. Mater. Interfaces*, 2016, **8**, 20534–20539.
23 Q. Dong, Q. Wang, Z. Dai, H. Qiu and X. Dong, *ACS Appl. Mater. Interfaces*, 2016, **8**, 26902–26907.
24 X. Liu, Y. Liu and L.-Z. Fan, *J. Mater. Chem. A*, 2017, **5**, 15310–15314.
25 Y. Guo, J. Tang, Z. Wang, Y.-M. Kang, Y. Bando and Y. Yamauchi, *Nano Energy*, 2018, **47**, 494–502.
26 L.-L. Wu, Q.-S. Wang, J. Li, Y. Long, Y. Liu, S.-Y. Song and H.-J. Zhang, *Small*, 2018, **14**, 1704035.
27 X. Zhang, S. Liu, Y. Zang, R. Liu, G. Liu, G. Wang, Y. Zhang, H. Zhang and H. Zhao, *Nano Energy*, 2016, **30**, 93–102.
28 S. Liu, X. Zhang, G. Wang, Y. Zhang and H. Zhang, *ACS Appl. Mater. Interfaces*, 2017, **9**, 34269–34278.
29 Y. Guo, J. Tang, H. Qian, Z. Wang and Y. Yamauchi, *Chem. Mater.*, 2017, **29**, 5566–5573.
30 M. K. Aslam, S. S. A. Shah, S. Li and C. Chen, *J. Mater. Chem. A*, 2018, **6**, 14083–14090.
31 X.-Y. Yu, Y. Feng, B. Guan, X. W. (David) Lou and U. Paik, *Energy Environ. Sci.*, 2016, **9**, 1246–1250.
32 P. Wang, Z. Xu, Y. Lin, L. Wan and B. Wang, *ACS Sustainable Chem. Eng.*, 2020, **8**, 8949–8957.
33 X. Xiao, C.-T. He, S. Zhao, J. Li, W. Lin, Z. Yuan, Q. Zhang, S. Wang, L. Dai and D. Yu, *Energy Environ. Sci.*, 2017, **10**, 893–899.
34 J. Song, C. Zhu, B. Z. Xu, S. Fu, M. H. Engelhard, R. Ye, D. Du, S. P. Beckman and Y. Lin, *Adv. Energy Mater.*, 2017, **7**, 1601555.
35 B. You, N. Jiang, M. Sheng, S. Gul, J. Yano and Y. Sun, *Chem. Mater.*, 2015, **27**, 7636–7642.
36 C. Guan, W. Xiao, H. Wu, X. Liu, W. Zang, H. Zhang, J. Ding, Y. P. Feng, S. J. Pennycook and J. Wang, *Nano Energy*, 2018, **48**, 73–80.
37 E. Hu, J. Ning, D. Zhao, C. Xu, Y. Lin, Y. Zhong, Z. Zhang, Y. Wang and Y. Hu, *Small*, 2018, **14**, 1704233.
38 S. Hu, S. Wang, C. Feng, H. Wu, J. Zhang and H. Mei, *ACS Sustainable Chem. Eng.*, 2020, **8**, 7414–7422.
39 K. Chen, R. Rajendiran, C. Deviprasath, S. Mathew, Y.-R. Cho, K. Prabakar and O. Lun Li, *ChemElectroChem*, 2022, **9**, e202200093.
40 S. Peng, F. Gong, L. Li, D. Yu, D. Ji, T. Zhang, Z. Hu, Z. Zhang, S. Chou, Y. Du and S. Ramakrishna, *J. Am. Chem. Soc.*, 2018, **140**, 13644–13653.
41 H. Xu, J. Cao, C. Shan, B. Wang, P. Xi, W. Liu and Y. Tang, *Angew. Chem.*, 2018, **130**, 8790–8794.
42 L. Zhuang, L. Ge, Y. Yang, M. Li, Y. Jia, X. Yao and Z. Zhu, *Adv. Mater.*, 2017, **29**, 1606793.
43 Y. Yan, P. Gu, S. Zheng, M. Zheng, H. Pang and H. Xue, *J. Mater. Chem. A*, 2016, **4**, 19078–19085.
44 K. Kawashima, R. A. Márquez, Y. J. Son, C. Guo, R. R. Vaidyula, L. A. Smith, C. E. Chukwuneke and C. B. Mullins, *ACS Catal.*, 2023, **13**, 1893–1898.
45 K. Kawashima, Y. J. Son, Z. Wang, R. F. Rose, R. A. Marquez-Montes, L. A. Smith, C. E. Chukwuneke and C. B. Mullins, *Meet. Abstr.*, 2023, **MA2023–02**, 3126.
46 A. E. F. Milton, K. Kawashima, Y. J. Son, W. J. Chang, Z. Wang, R. A. Marquez, R. F. Rose, D. J. Milliron and C. B. Mullins, *Meet. Abstr.*, 2024, **MA2024–02**, 4742.
47 R. A. Marquez, E. Kalokowski, M. Espinosa, J. T. Bender, Y. J. Son, K. Kawashima, C. E. Chukwuneke, L. A. Smith, H. Celio, A. Dolocan, X. Zhan, N. Miller, D. J. Milliron, J. Resasco and C. B. Mullins, *Energy Environ. Sci.*, 2024, **17**, 2028–2045.
48 C. G. Jones, M. W. Martynowycz, J. Hattne, T. J. Fulton, B. M. Stoltz, J. A. Rodriguez, H. M. Nelson and T. Gonen, *ACS Cent. Sci.*, 2018, **4**, 1587–1592.
49 W. Kabsch, *Acta Crystallogr. D*, 2010, **66**, 125–132.
50 O. V. Dolomanov, L. J. Bourhis, R. J. Gildea, J. a. K. Howard and H. Puschmann, *J. Appl. Crystallogr.*, 2009, **42**, 339–341.
51 G. M. Sheldrick, *Acta Crystallogr. A*, 2008, **64**, 112–122.
52 L.-M. Peng, *Micron*, 1999, **30**, 625–648.
53 S. U. Aashima, A. Arora, S. Gautam, S. Singh, R. J. Choudhary and S. K. Mehta, *RSC Adv.*, 2019, **9**, 23129–23141.
54 B. Shen, F. Wang and T. Liu, *Powder Technol.*, 2014, **253**, 152–157.
55 M. Liu, K.-A. Min, B. Han and L. Y. S. Lee, *Adv. Energy Mater.*, 2021, **11**, 2101281.
56 Y. Zhou, S. Ren, J. Yang, W. Liu, Z. Su, Z. Chen, M. Wang and L. Chen, *J. Energy Inst.*, 2021, **98**, 199–205.
57 F. Sun, G. Wang, Y. Ding, C. Wang, B. Yuan and Y. Lin, *Adv. Energy Mater.*, 2018, **8**, 1800584.
58 C. E. Chukwuneke, K. Kawashima, H. Li, R. A. Marquez, Y. Jun Son, L. A. Smith, H. Celio, G. Henkelman and C. Buddie Mullins, *J. Mater. Chem. A*, 2024, **12**, 1654–1661.
59 K. Kawashima, R. A. Márquez-Montes, H. Li, K. Shin, C. L. Cao, K. M. Vo, Y. J. Son, B. R. Wygant, A. Chunangad, D. H. Youn, G. Henkelman, V. H. Ramos-Sánchez and C. B. Mullins, *Mater. Adv.*, 2021, **2**, 2299–2309.

60 M. Shalom, D. Ressnig, X. Yang, G. Clavel, T. Patrick Fellinger and M. Antonietti, *J. Mater. Chem. A*, 2015, **3**, 8171–8177.
61 J. Liu, Y. Liu, X. Mu, H. Jang, Z. Lei, S. Jiao, P. Yan, M. G. Kim and R. Cao, *Adv. Funct. Mater.*, 2022, **32**, 2204086.
62 K. Kawashima, M. Hojamberdiev, H. Wagata, K. Yubuta, K. Domen and K. Teshima, *ACS Sustainable Chem. Eng.*, 2017, **5**, 232–240.
63 N. P. Dileep, J. Patel and Y. Pushkar, *Inorg. Chem.*, 2024, **63**, 8050–8058.
64 Y. Zhu, Z. Chen, H. Li, Q. Wang, X. Liu, Y. Hu, C. Su, R. Duan, S. Chen and L. Lan, *Sci. Rep.*, 2023, **13**, 3386.
65 M. Lammert, C. Glißmann, H. Reinsch and N. Stock, *Cryst. Growth Des.*, 2017, **17**, 1125–1131.
66 K. Tan, N. Nijem, P. Canepa, Q. Gong, J. Li, T. Thonhauser and Y. J. Chabal, *Chem. Mater.*, 2012, **24**, 3153–3167.
67 F.-L. Li, P. Wang, X. Huang, D. J. Young, H.-F. Wang, P. Braunstein and J.-P. Lang, *Angew. Chem.*, 2019, **131**, 7125–7130.
68 Infrared Spectroscopy Absorption Table, https://chem.libretexts.org/Ancillary_Materials/Reference/Reference_Tables/Spectroscopic_Reference_Tables/Infrared_Spectroscopy_Absorption_Table, accessed September 22, 2024.
69 C. C. L. McCrory, S. Jung, I. M. Ferrer, S. M. Chatman, J. C. Peters and T. F. Jaramillo, *J. Am. Chem. Soc.*, 2015, **137**, 4347–4357.
70 A. J. Bard, L. R. Faulkner and H. S. White, *Electrochemical Methods: Fundamentals and Applications*, John Wiley & Sons, 2022.
71 C. C. L. McCrory, S. Jung, J. C. Peters and T. F. Jaramillo, *J. Am. Chem. Soc.*, 2013, **135**, 16977–16987.
72 R. Jamil, R. Ali, S. Loomba, J. Xian, M. Yousaf, K. Khan, B. Shabbir, C. F. McConville, A. Mahmood and N. Mahmood, *Chem Catal.*, 2021, **1**, 802–854.
73 T. L. Cottrell, *The Strengths of Chemical Bonds*, Butterworths, London, 2nd edn, 1958.
74 Z. Huang, X. Liao, W. Zhang, J. Hu and Q. Gao, *ACS Catal.*, 2022, **12**, 13951–13960.
75 A. C. Garcia, T. Touzalin, C. Nieuwland, N. Perini and M. T. M. Koper, *Angew. Chem., Int. Ed.*, 2019, **58**, 12999–13003.
76 S. Lee, K. Banjac, M. Lingenfelder and X. Hu, *Angew. Chem., Int. Ed.*, 2019, **58**, 10295–10299.
77 C. Gu, H. Zhang, X. Wang and J. Tu, *RSC Adv.*, 2013, **3**, 11807–11815.
78 J. Guerrero-Contreras and F. Caballero-Briones, *Mater. Chem. Phys.*, 2015, **153**, 209–220.
79 A. C. Ferrari and J. Robertson, *Phys. Rev. B: Condens. Matter Mater. Phys.*, 2001, **64**, 075414.
80 Y. L. Lo and B. J. Hwang, *Langmuir*, 1998, **14**, 944–950.
81 L. A. Smith, K. Kawashima, R. A. Marquez and C. B. Mullins, *ACS Mater. Lett.*, 2024, **6**, 3190–3201.
82 W. Zheng, *Chem.: Methods*, 2023, **3**, e202200042.